Supplementary Information

This Supplementary Information file contains:

- Supplementary Notes
- Supplementary Figures 1 to 19
- Supplementary Table 1
- Supplementary Videos 1 to 8
- References

Supplementary Notes

Characteristics of the ionic electrode

The resistance and capacitance of the ionic conductors on the TPU substrate were tested by the digital LCR meter (AT3818, anbai, China). The tensile test was carried out on a single-arm tensile test machine (JHY-5000, Xingsuozhineng, China). During the bending test, the material was sandwiched between flexible acrylic sheets and the curvature was calculated by measuring the bending angle.

On a glass substrate, the pure ionic electrode was prepared and then sandwiched between two ITO sheets. Resistivity was characterized by the electrochemical impedance spectroscopy (CHI 660E electrochemical workstation). The resistance of the electrode was approximated by the high-frequency intercept of the semi-circle in the Nyquist diagram, and the resistivity of the ionic electrode was calculated by the equation:

$$\rho = \frac{RA}{d} \tag{1}$$

where is the resistivity, is the resistance, is the area, and is the thickness. The calculated resistivity was about 1657 Ω·m, the sheet resistance was about 23.7 MΩ calculated by the equation:

$$R_s = \frac{\rho}{d} \tag{2}$$

and the measured capacitance was 20 nF at 1 kHz. The time delay due to the capacitance of the dielectric and the resistance of the ionic electrode was about 0.474 seconds calculated by the equation

$$\tau = R_s C \tag{3}$$

The ionic electrode was tested for stability while stretched, and the resistance changed less than 3 times to its original value when stretched to 100%. In the bidirectional bending test, the resistance varied between 0.88 and 1.12 times from inward to outward bending, maintaining good stability. The freshly prepared device was directly exposed to air for 7 hours at room temperature, and the resistance increased only 0.62 times. Further, the resistance change of the electrode for 2000 cycles at 30% tensile strain was characterized, indicating that it possessed good cycling stability.

COMSOL simulation

COMSOL Multiphysics simulation was used to guide the optimization on the structure.

Electrohydrodynamics involves the coupling of electrostatics and hydrodynamics, which correspond to the electrostatic module and laminar flow module in COMSOL Multiphysics, respectively, and relies on the interaction of the dilute species transfer module. The driving force for EHD pumping is the electric body force. The electric body force density acting on a dielectric fluid with free space charge density under the action of electric field is given by equation:

$$f_e = \rho_e E - \frac{1}{2}E^2\nabla\varepsilon + \frac{1}{2}\nabla\left[E^2\rho\left(\frac{\partial\varepsilon}{\partial\rho}\right)_T\right] \tag{4}$$

where is the dielectric constant of the liquid, is the fluid density and is the temperature. The first term is the Coulomb force, the second term is the dielectric force, and the third is the electrostriction. Here, considering that EHD pumping acts on the single-phase, incompressible fluid, only Coulomb forces are considered.

In the electrostatics module, the magnetic field is negligible, and according to Gauss's law, the electric field is irrotational:

$$\nabla \times E = 0 \tag{5}$$

Which is the static version of Faraday's law. The relationship between the electric field and charge density is given by:

$$\nabla \cdot E = \frac{\rho_e}{\varepsilon} \tag{6}$$

The irrotational nature of the electric field can be represented by the potential field gradient of the electric field:

$$E = -\nabla V \tag{7}$$

According to the law of conservation of charge:

$$\frac{\partial\rho_e}{\partial t} + \nabla \cdot J = 0 \tag{8}$$

Where the current density is defined as the sum of the current density components within the control volume medium and due to the overall motion of the medium. Therefore, the current density is:

$$J = \mu_e\rho_e E + D\nabla\rho_e + \rho_e u + \sigma E \tag{9}$$

Where is the mobility of charge, is the diffusion coefficient, is the velocity of fluid and is the electric conductivity. At high electric fields, diffusion is negligible relative to charge migration. In the steady state case, a new charge conservation equation is obtained:

$$\nabla\left(\mu_e\rho_e E+\rho_e u+\sigma E\right)=0 \tag{10}$$

It is assumed that the fluid flow is laminar, steady, and incompressible, and that the fluid flow is governed by the continuity equation and the Navier-Stokes equation:

$$\begin{gathered}\nabla\cdot u=0\\ \rho\left[\frac{\partial u}{\partial t}+\left(u\cdot\nabla\right)u\right]=-\nabla p+\mu\nabla^2 u+f_e\end{gathered} \tag{11}$$

Where and is the pressure. The output pressure of EHD pumping can be solved from the above equations. For the conservation of charge, no physics in COMSOL represents the law of conservation of charge. However, the transport of diluted species is carried out using the Nernst-Planck equation for the conservation of chemical species concentrations:

$$\nabla\cdot\left(-D_i\nabla c_i+z_i\mu_{e,i}Ec_i\right)+u\cdot\nabla c_i=R_i \tag{12}$$

Where is the concentration of ions, is the valency of ions and is the reaction rate. With the diffusion coefficient set to zero, the charge density will be the concentration multiplied by Avogadro's number and the electric charge constant.

For electrostatics, the boundary conditions are straight forward, with a voltage applied at the collector and a ground at the emitter. At the fingers of electrodes, the rate of electron generation and annihilation is characterized by a normal current density and closely related to the power consumption of the system. For the configuration without the supporting layer, the surface of the coupled current in a pair of forked fingers was limited to only the two faces (the coupling area on a single finger was 0.05×6 mm^2) directly opposite each other with the smallest distance, with the normal current density being $\pm 5 \times 10^{-6}$ A/m^2 with an initial concentration of 0 mol/m^3. For the structure with the supporting layer, the area of the upper and lower sides facing each other was considered, thus the coupling area per individual finger was 0.75×8 mm² which is 20 times that of the former, implying that power consumption is increased by a factor of 20. Therefore, under the same power consumption, the normal current density for the configuration with the supporting layer was set to $\pm 2.5 \times 10^{-7}$ A/m^2. The field emission efficiency of electrodes is closely related to the electric field and the electrode material. To simplify the computation, we maintained a consistent emission efficiency for the electrodes under different electric fields. Although this resulted in a linear variation of the output pressure with voltage, it did not affect the increase or decrease of the

pressure outputs.

The dielectric liquid used for the simulation was set with three parameters, kinetic viscosity, density and relative dielectric constant and their values were 320 Pa·s, 1400 kg/m^3 and 7.2 respectively. To solve for the steady state blocking pressure, the starting concentration of the dielectric fluid is 0.01 mol/m^3, the inlet of the pump is an open boundary condition with positive stress of 0 N m^{-2}, and the outlet is a velocity boundary condition with output velocity of 0 m/s. For the pressure data obtained by simulation, the variation of the channel height was achieved by adjusting the height of the support layer, and the output pressures depicted in Fig. 2E and Fig. 2H were derived from the steady-state average values at the outlet cross-section.

The dimension of the fluid domain within the model was 67 mm × 8 mm (length × width), with the height being determined collectively by the electrode thickness and the supporting layer. The electrodes were positioned at the central location of the model.

Charge injection based on ionic conductors

For EHD systems based on electronic conductors, charge injection into the liquid is typically associated with chemical reactions at the electrode/liquid interfaces, which is one case for the generation of current in the circuit[1]. The second case is that the dissociation in the liquid causes the generation of charge carriers, which produces a current within the circuit and is independent of the type of electrode material[2]. We measured the current of the EHD system based on solid-state ionic conductors. The electrical double layer at the interface between electronic and ionic conductors exhibits a high capacitance, enabling a rapid surge in current within a short period of the applied bias. Here, we focused on the current characteristics of the EHD system at the steady state. As the dissociation in the liquid require a certain high voltage, the current contributed from the charges with the dissociation increases nonlinearly with the electric field under strong electric fields. As shown in Supplementary Fig. 2B, a large increase in the current was observed at 8 kV. Consequently, the linear increase of current under lower electric field was attributed to the charge injections from the ionic conductors.

Further, we have designed experiments to obtain further evidence of ion injection and migration from the negative to the positive ionic electrodes. Exposed ionic electrodes with 15 pairs of forked fingers were prepared on top of a TPU film and immersed in the working fluid. The ionic electrode

was placed upwards at a distance of about 1 mm from the liquid level. Under electrical bias, traces of ions injected from the solid-state ionic conductor and emitted from the negative toward the positive have been observed under the microscope, as shown in Supplementary Fig. 2E. We carried out an Energy-dispersive X-ray spectroscopy (EDS) analysis on the elemental compositions of the traces, confirming that sulfur and nitrogen elements of the anions from solid-state ion electrodes were present in the traces.

The equivalent electric circuit model of the transparent EHD pump

Within the EHD system incorporating ionic conductors, two distinct interfaces exist: the solid-solid interface between the ionic conductor and the electronic conductor, and the solid-liquid interface between the ionic conductor and the dielectric liquid, Supplementary Fig. 5. Three primary charge carriers are present, including electrons in the electronic conductors, ions in the ionic conductors, and injected ions and dissociated ions in the dielectric liquids. Under low electric fields, dissociated ions are not likely to be present in the dielectric liquid. And its resistance is more than five orders of magnitude larger than that of the ionic conductors. Consequently, the rapid growth of transient current is due to the electric double layer at the solid-solid interfaces. The current gradually decline to a stabile value, during which the electric double layer continuously charges to couple the current in the circuit. Under sufficiently strong electric fields, dissociation will take place in the dielectric liquid, contributing additional charge carries and increasing the electrical conductivity of the liquid. The dissociated ions in the liquid migrate under the influence of the electric field to the solid-liquid interface, forming an electrical double layer. Due to the migration lag of charge carriers within the ionic conductors, a secondary growth of the current was observed under the voltage above 5 kV, Supplementary Fig. 5B.

Efficiency estimation of the pump

For pumps without mechanical friction, under constant operating conditions, there is a linear relationship between and the maximum energy efficiency can be calculated as[3]

$$eff = \frac{\Delta p_{\max} Q_{\max}}{4 P_{\text{in}}} \tag{13}$$

The maximum pressure is obtained when there is no flow at the outlet and the maximum flow rate is obtained when there is no pressure difference between the inlet and outlet. Based on this, we

estimated the energy efficiency of the pump with 15 pairs of forked fingers to be approximately 0.5% at an operating voltage of 8 kV. When the pump with 20 pairs of forked fingers operated at 12 kV, the current was less than 0.04 mA and the max power consumption was 0.48 W.

Analysis of the bidirectional characteristics of the pump

With the ionic electrodes, which have a different charge migration characteristic compared to the electronic electrodes, the output performance was attributed to the charging and discharging characteristics of the solid-state ionic electrodes. After the pump worked for a few seconds at a certain electric field, charge accumulation occurred at the electrode interfaces, while polarization occurred within the ionic electrodes. Consequently, when a reverse electric field of the same magnitude and duration was applied, the effective electric field across the working fluid was reduced due to the residual electric field in the ionic electrodes. This reduction in the effective electric field led to a decreased pressure outputs when the applied electric field was reversed.

Supplementary Figures

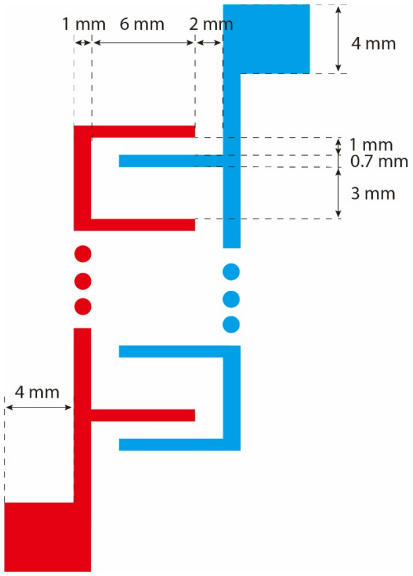

Supplementary Fig. 1. Schematic of the forked finger electrode. The electrode is centrosymmetric.

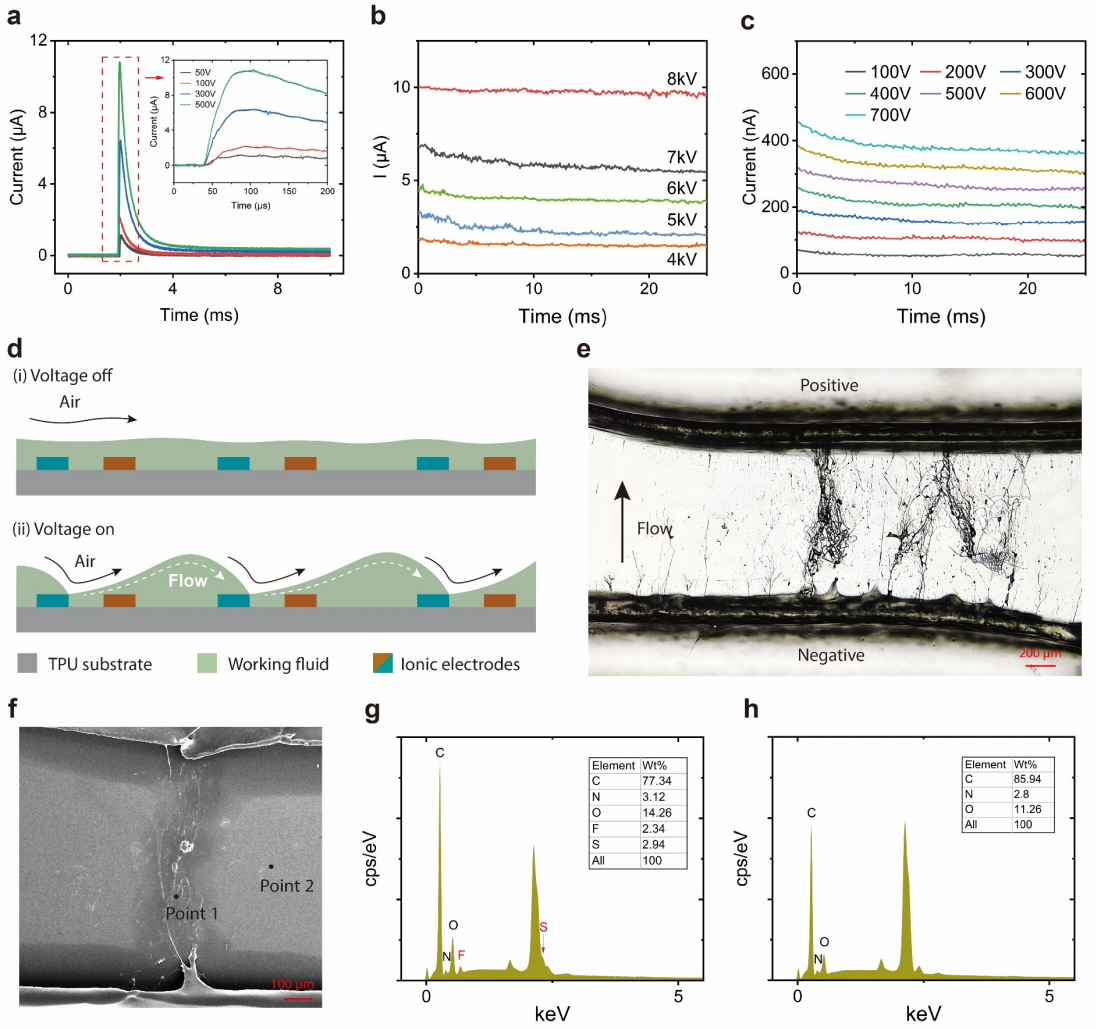

Supplementary Fig. 2. Current characteristics of the pump and ion injection process. The pump contains 20 pairs of forked fingers. **a**, Transient current characteristics under low electric fields. **b**, Steady current characteristics under high electric fields. **c**, Steady current characteristics under low electric fields. **d**, Schematic diagram of the EHD system exposed to air. **e**, Traces of ion injection from the negative ionic electrode and ion transport to the positive ionic electrodes, observed under optical microscope. **f**, SEM of the traces caused by ion injection. **g**, EDS analysis at point 1. **h**, EDS analysis at point 2.

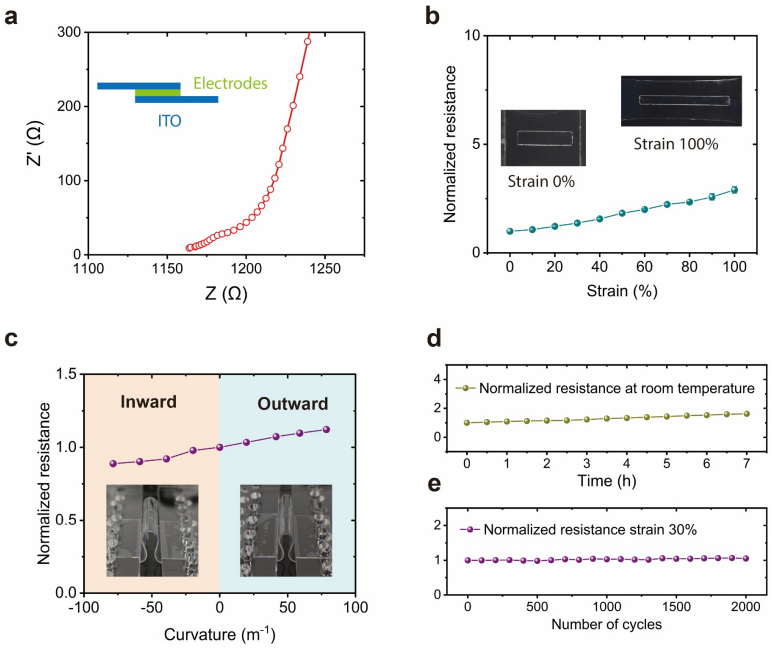

Supplementary Fig. 3. The electrochemical and electromechanical properties of the ionic electrodes. a, Electrochemical impedance spectroscopy measurements of the ionic conductor. The ionic conductor was sandwiched between two ITO sheets with dimensions: length × width × thickness = 10 mm × 10 mm × 0.07 mm. **b**, Resistance of the ionic electrode as a function of uniaxial tensile strain up to 100%. **c**, Resistance of the ionic electrode when changing from an inward bending curvature of 78.5 m^{-1} to an outward bending curvature of 78.5 m^{-1}. **d**, Resistance of the ionic electrode exposed in air for 7 hours. **e**, Cyclic stretching test of the ionic electrodes at the strain of 30% for 2000 cycles**.**

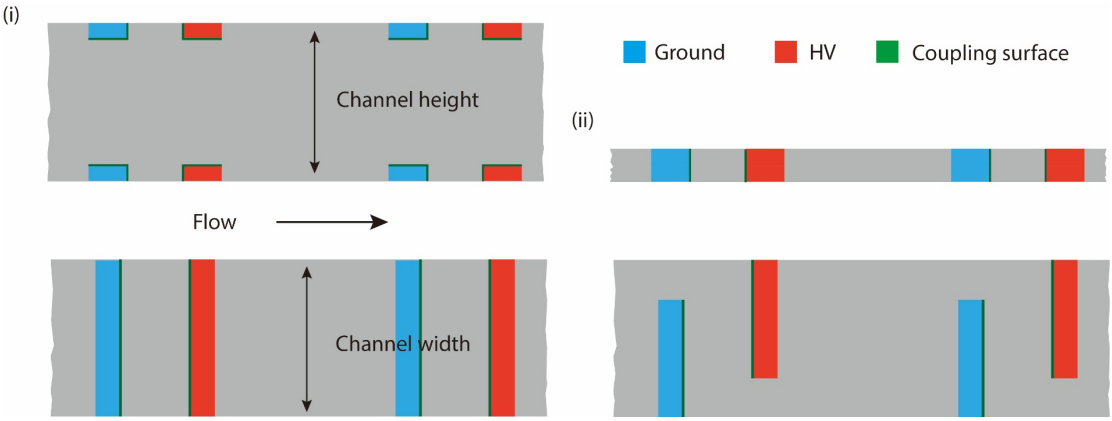

Supplementary Fig. 4. The current-coupling surfaces of the simulation model. (i) Model with the support layer. (ii) Model without the support layer**.**

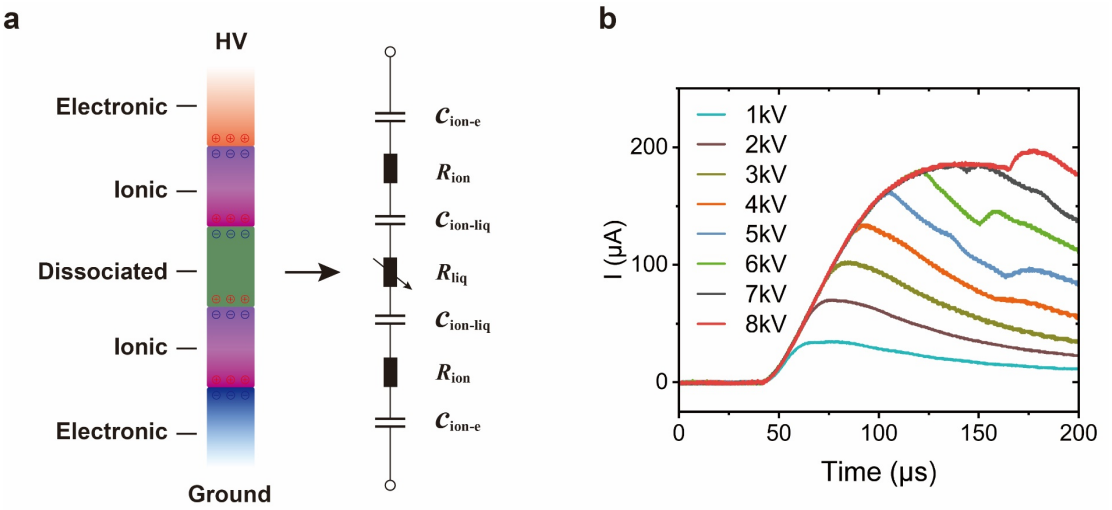

Supplementary Fig. 5. Electric circuit model and current characteristics of the transparent EHD pump. a, The circuit model of the transparent EHD pump. **b**, The current characteristics of the transparent EHD pump.

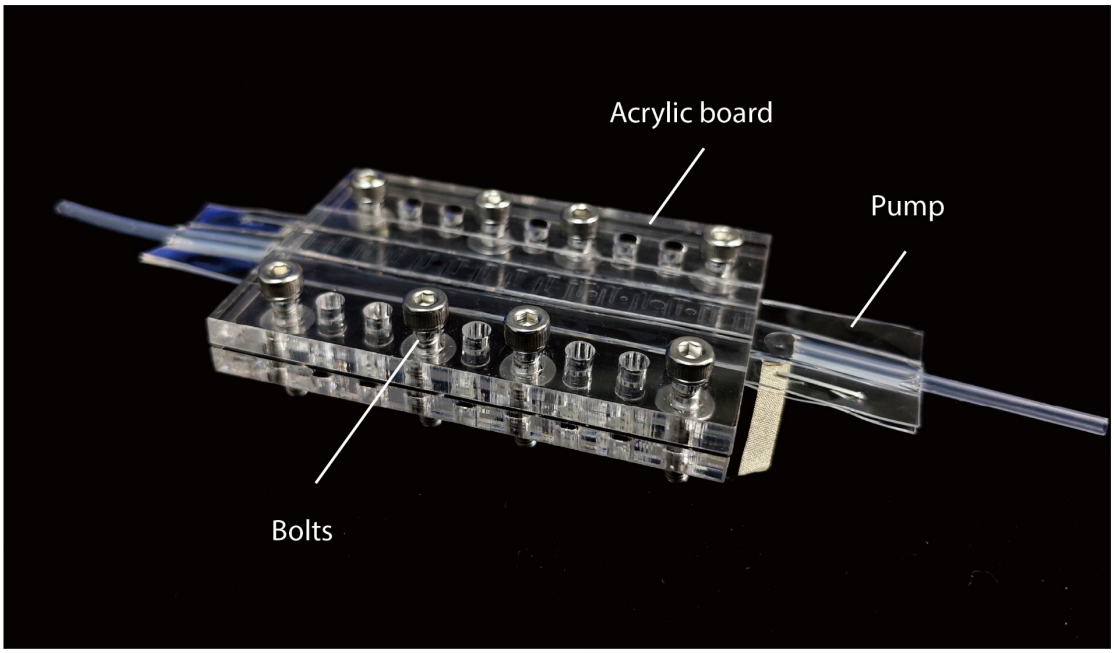

Supplementary Fig. 6. The device that limits the expansion of the pump. The device consisted of two 4 mm thick acrylic plates, between which the pump was clamped and fastened with bolts.

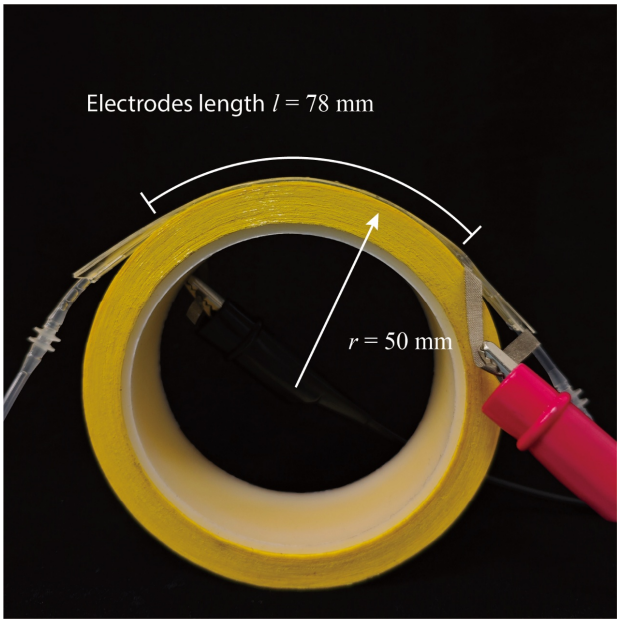

Supplementary Fig. 7. Image of the pump attached to a support with a radius of 50 mm. The bending angle was calculated from the arc length of the electrode bend and the radius of the support, and tests were performed on different supports to obtain the data. The effective electrode length l is defined as the length of the interfinger in the direction of the fluid channel.

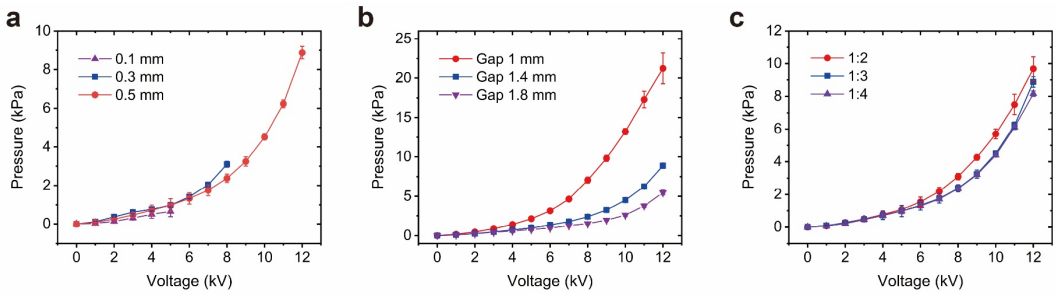

Supplementary Fig. 8. Pressure output curves of the pump in different situations. Unless otherwise specified, the thickness of the TPU film was 0.5 mm, the width of the gap was 1.4 mm, and the ratio of the gap was 1:3 and all error bars represent the standard deviation of the measurements for three pumps. **a**, Pressure output curves of the pump at different film thicknesses. The thicker TPU substrate films can withstand larger electric fields, and thus the higher the pressure outputs. **b**, Pressure output curves of the pump at different gap widths. The wider the electrode gap, the smaller the electric field at the same voltage, which reduces the pump outputs. **c**, Pressure output curves of the pump at different gap ratios. At different gap ratios, a smaller ratio would theoretically weaken the interaction of two neighboring pump units thus increasing output, but would mean longer fluid passages and cause a greater susceptibility to expansion, reducing output pressure.

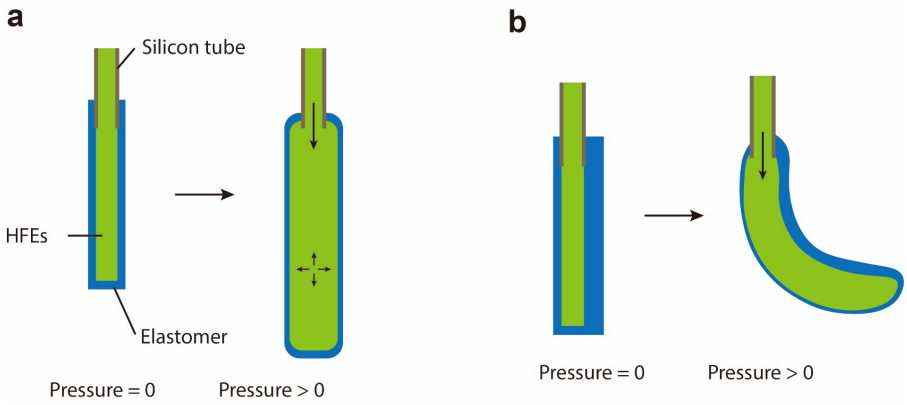

Supplementary Fig. 9. Structure diagram of the fiber actuators. a, The coaxial fiber actuators. **b**, The non-coaxial fiber actuators.

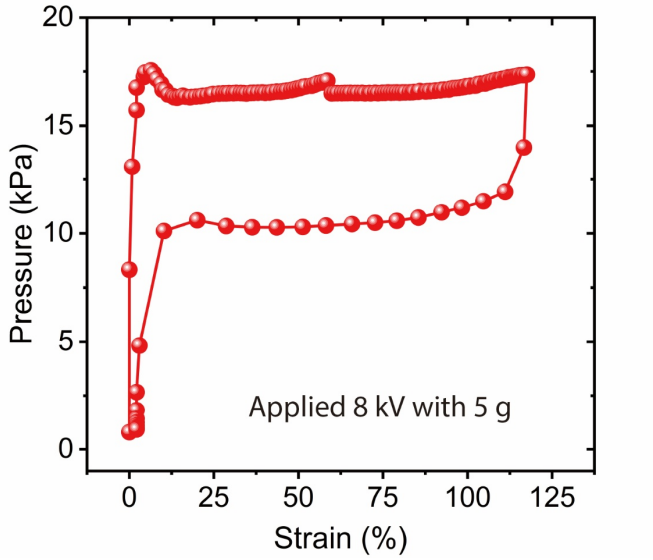

Supplementary Fig. 10. The relationship between the pressure inside the actuator and the strain in the vertical.

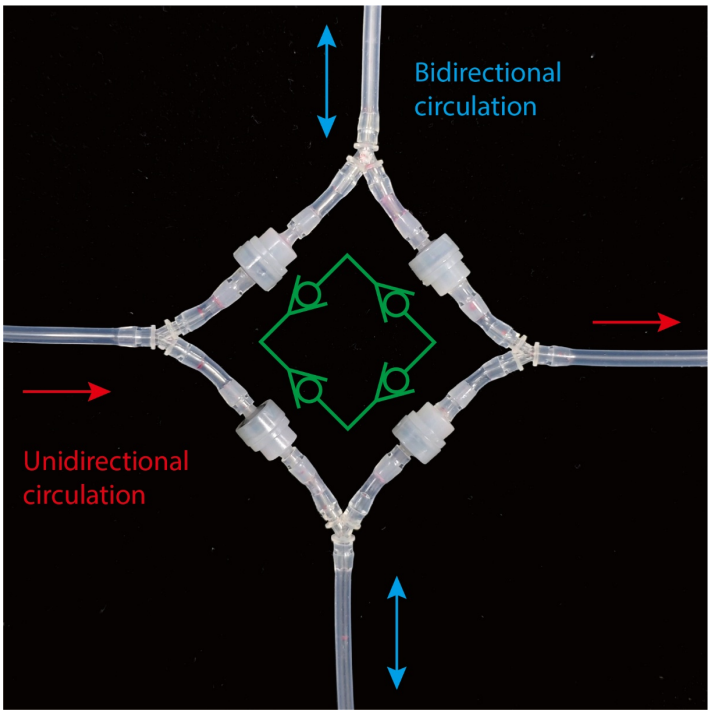

Supplementary Fig. 11. The connections of combined check valves. Combined check valves can convert bidirectional pumping (blue circuit) into unidirectional circulation (red circuit) in a given circuit.

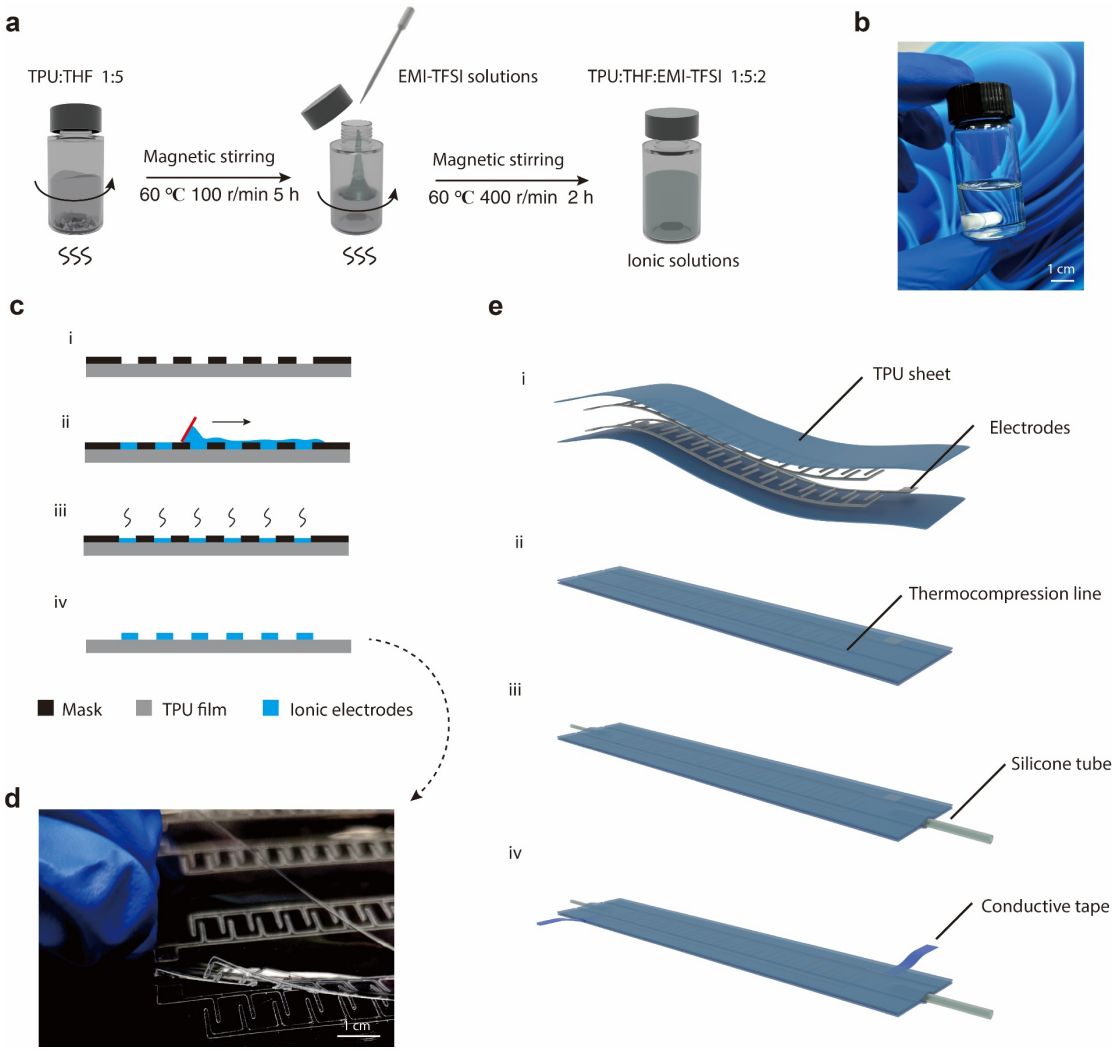

Supplementary Fig. 12. The preparation process of the transparent EHD pump. a, Preparation process of ionic electrode solution. **b**, A photograph of the prepared transparent ionic electrode solution. **c**, The process of patterning the ionic electrode onto the TPU substrate. **d**, A photograph of the ionic electrode that has completed patterning onto the TPU substrate. **e**, The assembly process of the transparent EHD pump.

Supplementary Fig. 13. Image of the electric scraper used for hot pressing operation.

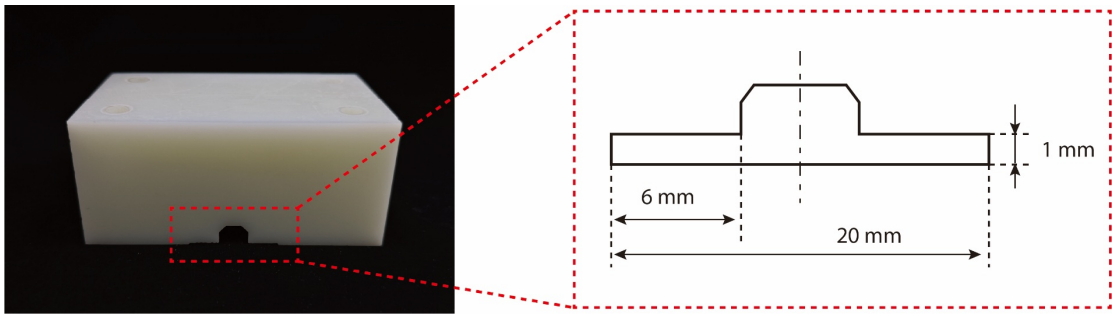

Supplementary Fig. 14. Images and dimensions of the fixture used for tensile testing. The fixture was designed to clamp the pump and keep the fluid passages open.

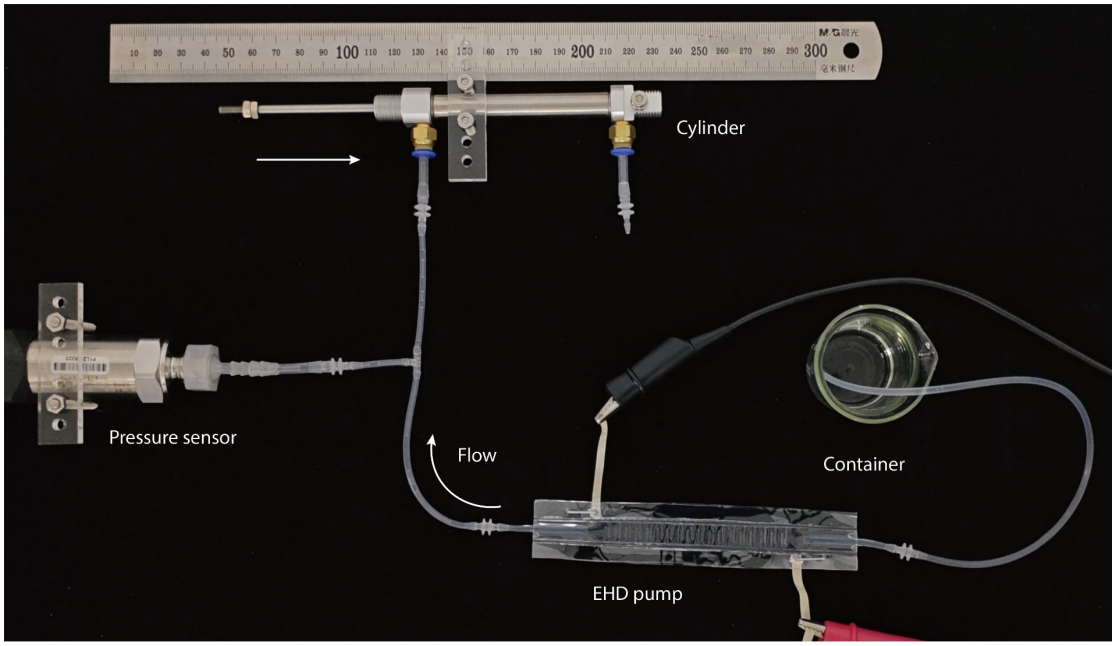

Supplementary Fig. 15. The connections of the system when the pump drove the cylinder without load.

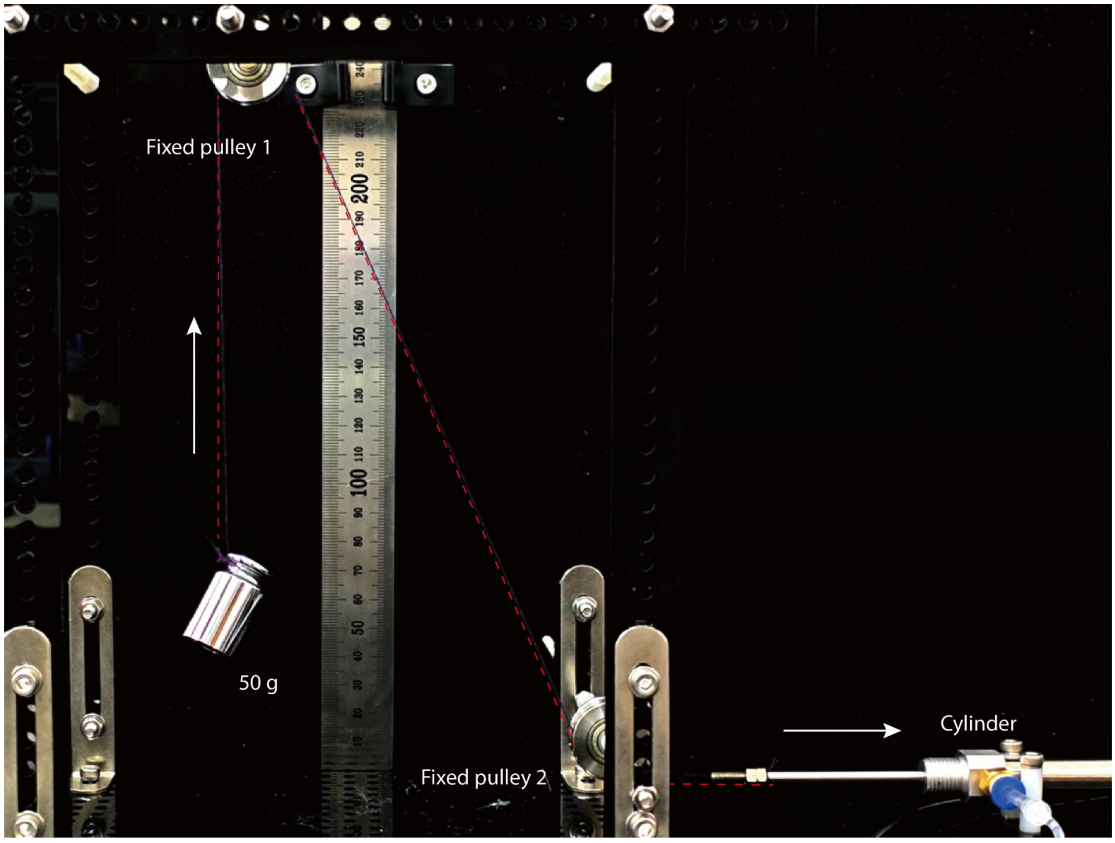

Supplementary Fig. 16. The connections of the system when the pump drove the cylinder at a load of 50 g.

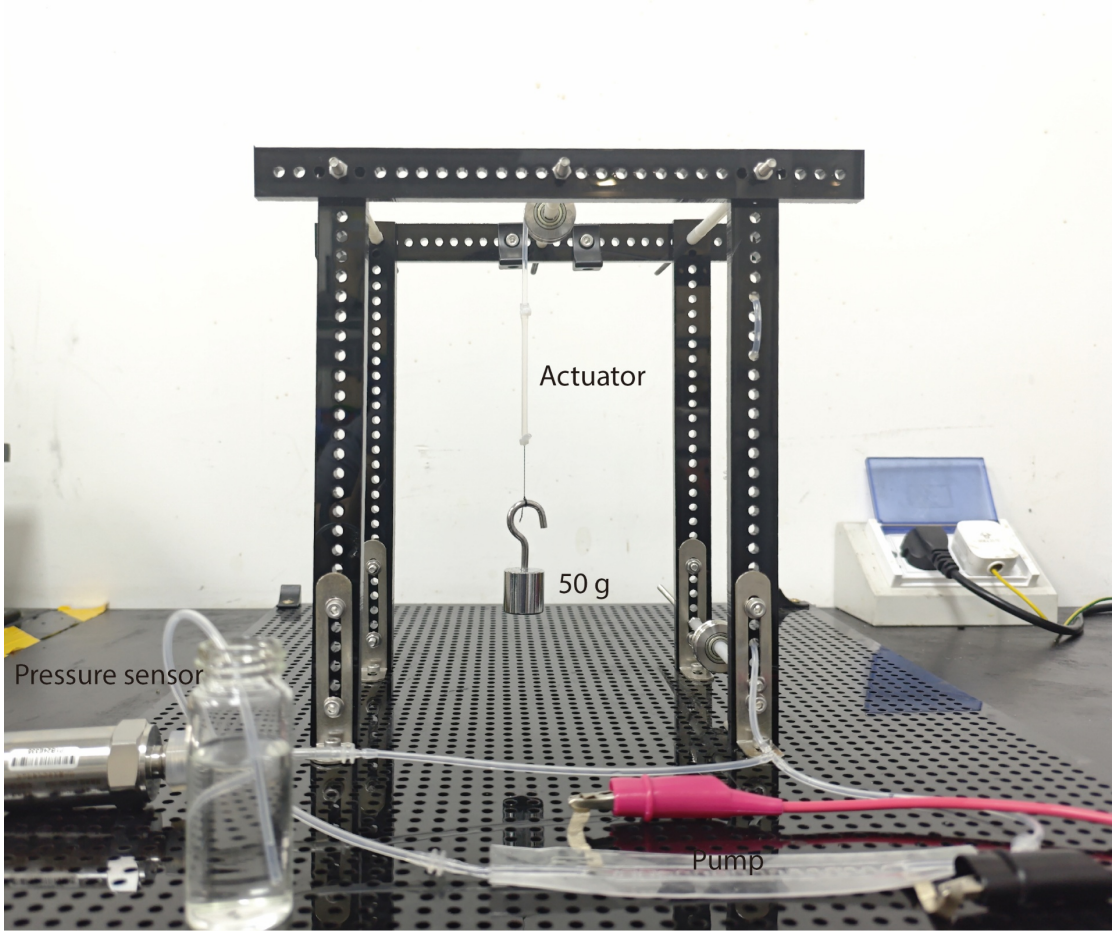

Supplementary Fig. 17. The connections of the system when the pump drove the Ecoflex fiber actuators.

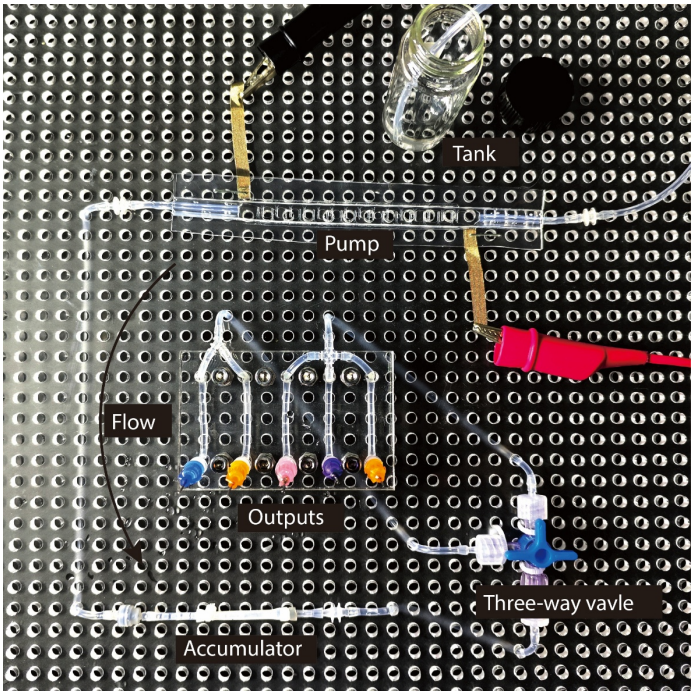

Supplementary Fig. 18. The connections of the system when the pump was integrated into the microfluidic system.

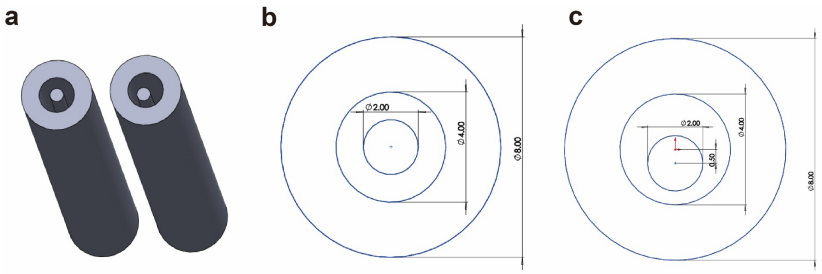

Supplementary Fig. 19. Image of the 3D-printed mold of the Ecoflex fiber actuator. a, The 3D model of the two molds. **b**, Image of the cross-sectional dimensions of the coaxial mold. **c**, Image of the cross-sectional dimensions of the non-coaxial mold.

Supplementary Table

Supplementary Table 1. Comparison of performances on reported soft pumps.

Pump type	Reference	Fully transparent	Max strain (%)	Max pressure (kPa)	Max flowrate (ml/min)	Mass (g)	Power consumption (W)	Max efficiency (%)
EHD	This work	Yes	200	71	5.1	4	0.48	0.5
	Stretchable pump[4]	No	50	14	6	1	0.17	N/A
	Fiber pump[5]	No	25	80	45	1.2	0.71	2.1
	Self-healing pump[6]	No	N/A	9.2	423	3	0.03	N/A
	Silicone pump[7]	No	30	4.1	161	5.3	N/A	N/A
DEA	Compact DEA pump[8]	No	N/A	12.5	39	12-15	1.16	8.3
	Pocket pump[9]	No	N/A	7.5	340	2.4	1.58	0.35
	EPP pump[10]	No	N/A	2.34	161	5.3	0.5	46.5
	Heterogeneous pump[11]	No	80	2.75	3.25	1	0.21	N/A
	EBM pump[12]	No	40	6	630	N/A	N/A	20
	Trielectrode pump[13]	No	N/A	15.96	330	11.2	0.12	4.92
Combustion	Combustion pump[14]	No	N/A	60	40	N/A	N/A	N/A

Supplementary Videos

Supplementary Video 1

Pumping at 10 kV and generating a fluid jet.

Supplementary Video 2

Driving the mini-cylinder without load.

Supplementary Video 3

Driving the mini-cylinder at 50 g load.

Supplementary Video 4

Actuating the coaxial fiber actuator without load.

Supplementary Video 5

Actuating the coaxial fiber actuator at 50 g load.

Supplementary Video 6

Actuating the non-coaxial fiber actuator.

Supplementary Video 7

The work operated by integrating the pump into the microfluidic system.

Supplementary Video 8

Fluidic-electric coupling-based system control strategy realized by the pump.

References

1. Suh, Y. K. Modeling and simulation of ion transport in dielectric liquids - Fundamentals and review. IEEE Transactions on Dielectrics and Electrical Insulation 19, 831–848 (2012).

2. Onsager, L. Deviations from Ohm's Law in Weak Electrolytes. The Journal of Chemical Physics 2, 599–615 (1934).

3. Microfluidic Technologies for Miniaturized Analysis Systems. (Springer US, Boston, MA, 2007). doi:10.1007/978-0-387-68424-6.

4. Cacucciolo, V. et al. Stretchable pumps for soft machines. Nature 572, 516–519 (2019).

5. Smith, M., Cacucciolo, V. & Shea, H. Fiber pumps for wearable fluidic systems. Science 379, 1327–1332 (2023).

6. Tang, W. et al. Customizing a self-healing soft pump for robot. Nat Commun 12, 2247 (2021).

7. Kanno, R. et al. Silicone-based highly stretchable multifunctional fiber pumps. Sci Rep 14, 4618 (2024).

8. Xu, S., Nunez, C. M., Souri, M. & Wood, R. J. A compact DEA-based soft peristaltic pump for power and control of fluidic robots. Science Robotics 8, eadd4649 (2023).

9. Jiang, S., Tang, C., Dong, X., Liu, X.-J. & Zhao, H. Soft Pocket Pump for Multi-Medium Transportation via an Active Tubular Diaphragm. Advanced Functional Materials 33, 2370298 (2023).

10. Diteesawat, R. S., Helps, T., Taghavi, M. & Rossiter, J. Electro-pneumatic pumps for soft robotics. Science Robotics 6, eabc3721 (2021).

11. Wang, L. et al. A Stretchable Soft Pump Driven by a Heterogeneous Dielectric Elastomer Actuator. Advanced Functional Materials n/a, 2411160 (2024).

12. Sîrbu, I. D. et al. Electrostatic bellow muscle actuators and energy harvesters that stack up. Science Robotics 6, eaaz5796 (2021).

13. Lin, Y. et al. A Compact, High-Performance, and Deformation-Resilient Trielectrode Electrostatic Soft Pump for Soft Robotics. Advanced Intelligent Systems 2400423 (2024) doi:10.1002/aisy.202400423.

14. Stergiopulos, C. et al. A Soft Combustion-Driven Pump for Soft Robots. in (American Society of Mechanical Engineers Digital Collection, 2014). doi:10.1115/SMASIS2014-7536.